$K\beta$ resonant x-ray emission spectra in MnF_2

M. Taguchi and J. C. Parlebas
IPCMS-GEMM, UMR7504, CNRS, 23, rue du Loess, 67037 Strasbourg, France

T. Uozumi
College of Engineering, University of Osaka Prefecture, Gakuen-cho, Sakai 593, Japan

A. Kotani
Institute for Solid State Physics, University of Tokyo, Roppongi, Minato-ku, Tokyo 106, Japan

C.-C. Kao
National Synchrotron Light Source, Brookhaven National Laboratory, Upton, New York 11973

(Received 20 May 1999)

We report experimental and theoretical results on Mn $K\beta$ resonant x-ray emission spectra ($K\beta$ RXES) at the pre-edge region of *K*-edge x-ray absorption spectroscopy in a powdered MnF_2 sample. The experimental results are studied theoretically in terms of coherent second-order optical process, using a MnF_6^{-4} cluster model with the effects of intra-atomic multiplet coupling and interatomic hybridization in the space of three configurations and taking into account both the Mn $1s$-$3d$ quadrupole excitation and the Mn $1s$-$4p$ dipole excitation. The agreement between theory and experiment is good. Moreover, we show that if the sample is a single crystal the resonant x-ray emission spectroscopy caused by the quadrupole excitation has a strong sensitivity to the angle of the incident photon.

I. INTRODUCTION

High-energy spectroscopy is a powerful tool in the study of electronic states of strongly correlated systems. In general, there are two categories in high-energy spectroscopy. One is a first-order optical process like x-ray absorption spectroscopy (XAS) and x-ray photoemission spectroscopy (XPS). These spectroscopies have made a great contribution to the development of solid state physics.[1–6] The other is a second-order optical process like resonant x-ray emission spectroscopy (RXES) and normal x-ray emission spectroscopy (NXES), where the incident photon energy is taken near the absorption threshold for RXES but it is well above the threshold for NXES. Especially, RXES is making a remarkable progress recently, because of a high brilliance of new synchrotron radiation sources.

The spectral function of RXES is represented by two independent variables, the incident photon energy Ω and the emitted photon energy ω. In many experimental observations, the spectrum of RXES is measured as a function of ω with fixed values of Ω, and then the spectrum reflects the radiative transition from a specific intermediate state (determined by Ω) to final states of the second-order optical process. RXES of strongly correlated electron systems, such as $3d$ transition-metal compounds and $4f$ rare-earth compounds, have been investigated extensively both experimentally and theoretically,[7–15] and we have obtained important information about the electronic states. Typical examples are the Dy $4d\rightarrow 4f\rightarrow 4d$ RXES for DyF_3 (Ref. 10) and the Ce $3d\rightarrow 4f\rightarrow 3d$ RXES for CeO_2.[8,9,13] In the $4d\rightarrow 4f\rightarrow 4d$ RXES for DyF_3, the most important effect is an intra-atomic multiplet coupling and then the free atomic calculation can reproduce the experimental data very well.[14] Also, in the $3d\rightarrow 4f\rightarrow 3d$ RXES for CeO_2, the effect of interatomic covalency hybridization between localized $4f$ electrons and the O $2p$ valence band is very important.[8,9,13]

On the other hand, when ω is fixed and RXES is represented as a function of Ω, we have the so-called excitation spectrum. By fixing ω at a peak position of NXES, excitation spectra have recently been investigated quite extensively both experimentally and theoretically.[16–24] In excitation spectra of the Mn $K\beta$ RXES at *K*-edge region for MnF_2 and MnO, a quite sharp structure can be observed as compared to the conventional x-ray absorption spectra. This effect allows us to see small double pre-edge peaks at *K*-edge XAS. Taguchi *et al.*[22,23] analyzed these peaks by taking into account the quadrupole transition ($1s\rightarrow 3d$), where the emitted photon energy was fixed at the main and satellite peaks in $K\beta$ NXES. The agreement between the calculated and experimental results was satisfactory.

In the present paper, we study the Mn $K\beta$ RXES at the same region (i.e., at the pre-edge region of *K*-edge XAS) but by fixing the incident photon energy at the double pre-edge peaks in *K*-edge XAS. The aim of the present paper is not only to compare the experimental and theoretical results but also to present a theoretical prediction on how the Mn $K\beta$ RXES spectra change with the change of the incident photon direction (incident angle dependence) in the case of quadrupole excitation. Since this incident angle dependence is quite different from that in the case of dipole excitation, the RXES will be a useful tool in separating the quadrupole and dipole contributions if they coexist in the pre-edge region.

The paper is organized as follows: Sec. II describes the experimental arrangement and the experimental results. The model and the formalism used in this analysis are given in

Sec. III. Section IV shows calculated results and compares those with experimental results. The angle dependence of RXES and the relation between RXES and NXES are also shown. Section V is devoted to the conclusion of this study.

II. EXPERIMENT

The experiment was performed at the X21 hybrid wiggler beamline at the National Synchrotron Light Source. The beamline consists of a water-cooled four-crystal dispersive Si(220) monochromator with miscut angle of $-16°, 0°, 0°, +16°$, followed by a bent cylinder double-focusing mirror. The monochromator is tunable from 5 to 10 keV, and the energy resolution of the monochromator is 0.2 eV for the whole tuning range.[25] The emission spectra was measured by a 1-m Rowland circle crystal spectrometer, using a spherically bent Si(440) analyzer crystal. The analyzer energy scale was calibrated against that of the monochromator by measuring the elastic scattering line from the sample to ensure that the two energy scales are consistent. And, the total energy resolution of the experiment is 0.4 eV, determined by the energy width of the elastic line. Pure MnF_2 powdered, compacted into a 5 mm diameter and 1 mm-thick disk, was used in the experiment. All spectra reported here were measured at 90° scattering angle and in the horizontal plane to reduce scattering background.

Figures 1(a) and 1(b) show the Mn *K*-edge absorption spectrum of the powdered MnF_2 sample. Figure 1(a) shows the near-edge part of the absorption spectrum, and Fig. 1(b) an expanded view of the pre-edge part of the same spectrum. With improved monochromator resolution, two spectral features, roughly located at 6539.9 and 6540.6 eV, are observed in the well-known pre-edge region, although they cannot be resolved clearly due to the core-hole lifetime broadening. The peak positions determined by fitting the pre-edge region of the spectrum with two Lorentzians plus a third order polynomial are 6539.83 and 6540.69 eV, respectively. Because of the uncertainty in the background line shape, these parameters should be used with care. The double-peaked pre-edge feature is assigned to quadrupole transitions from Mn $1s$ to the crystal-field split $3d$ states, although the exact nature of the transition is still an unresolved issue and will be addressed later in the theory section.

Figure 1(c) shows a series of emission spectra taken with the incident photon energy tuned to 6539.9 eV (A), and 6540.6 eV (B), 6545 eV (C), 6550 eV (D), 6554 eV (E), and 6600 eV, respectively. The incident energies, except 6600 eV, are also indicated in the absorption spectrum. Spectrum taken at 6600 eV is the typical Mn $K\beta$ NXES since the incident energy is much higher than the absorption edge. Spectra (A) to (E), on the other hand, are RXES measured by using either the $1s$ to $4p$ dipole transition (C)-(E) or the $1s$-$3d$ quadrupole transition (A)-(B) to excite the intermediate states. Except for a small energy shift, spectra (A) and (B) are very similar, both characterized by a double-peak feature between 6490 and 6495 eV, a small shoulder below 6490 eV, and a broad feature extending from 6475 to 6485 eV. In fact, the two spectra are completely aligned if the scattering intensity is plotted as a function of the final-state energy; and the only difference between (A) and (B) is the relative intensities between the two stronger peaks. And, the final state energies are 47.8, 49, and 51.2 eV for the double peaks and the shoulder, respectively. On the other hand, spectra (C)-(E) show very different behavior in comparison with spectra (A) and (B). The lineshape evolves from (C) to (E) towards that of the normal fluorescence spectrum. And, there is also strong but nonlinear dispersion with respect to the incident energy of these spectra.

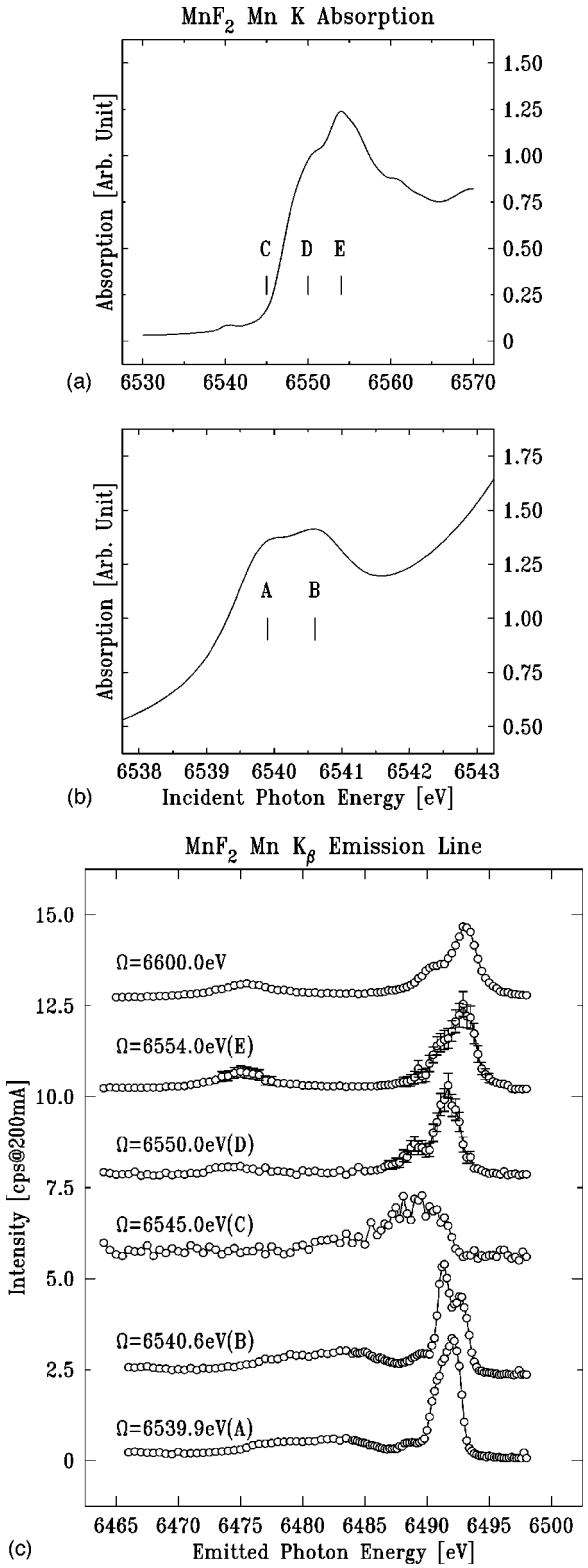

FIG. 1. Experimental results of (a) Mn *K*-XAS in the near edge region, (b) that in the pre-edge region, and (c) Mn $K\beta$ RXES.

III. FORMULATION

In order to describe Mn $1s$, $3p$, and $3d$ states and F $2p$ ligand states of MnF_2, we use the model of Refs. 22 and 23, namely a MnF_6^{-4} cluster model. The symmetry of the cluster is taken approximately as the O_h symmetry.

The Hamiltonian for the calculation of Mn $K\beta$ RXES due to the quadrupole transition (where a $1s$ core electron is excited to the $3d$ states) is given by

$$\begin{aligned} H=&\sum_{\Gamma,\sigma}\varepsilon_{3d}(\Gamma)d^{\dagger}_{\Gamma\sigma}d_{\Gamma\sigma}+\sum_{m,\sigma}\varepsilon_{3p}p^{\dagger}_{m\sigma}p_{m\sigma}\\ &+\sum_{\sigma}\varepsilon_{1s}s^{\dagger}_{\sigma}s_{\sigma}+\sum_{\Gamma\sigma}\varepsilon_{p}(\Gamma)a^{\dagger}_{\Gamma\sigma}a_{\Gamma\sigma}\\ &+\sum_{\Gamma,\sigma}V(\Gamma)(d^{\dagger}_{\Gamma\sigma}a_{\Gamma\sigma}+a^{\dagger}_{\Gamma\sigma}d_{\Gamma\sigma})\\ &+U_{dd}\sum_{(\Gamma,\sigma)\neq(\Gamma',\sigma')}d^{\dagger}_{\Gamma\sigma}d_{\Gamma\sigma}d^{\dagger}_{\Gamma'\sigma'}d_{\Gamma'\sigma'}\\ &-U_{dc}(1s)\sum_{\Gamma,\sigma,\sigma'}d^{\dagger}_{\Gamma\sigma}d_{\Gamma\sigma}(1-s^{\dagger}_{\sigma'}s_{\sigma'})\\ &-U_{dc}(3p)\sum_{\Gamma,m,\sigma,\sigma'}d^{\dagger}_{\Gamma\sigma}d_{\Gamma\sigma}(1-p^{\dagger}_{m\sigma'}p_{m\sigma'})\\ &+H_{\text{multiplet}}, \end{aligned} \tag{3.1}$$

where $\varepsilon_{3d}(\Gamma)$, ε_{3p}, ε_{1s}, and $\varepsilon_p(\Gamma)$ represent the energies of Mn $3d$, Mn $3p$, Mn $1s$, and F $2p$ ligand states, respectively, with the irreducible representation $\Gamma(=e_g$ and $t_{2g})$ of the O_h symmetry. The indices m and σ are the orbital and spin states. $V(\Gamma)$, U_{dd}, $-U_{dc}(1s)$, and $-U_{dc}(3p)$ are the hybridization between Mn $3d$ and F $2p$ ligand states, the Coulomb interaction between Mn $3d$ states and the Coulomb interaction between Mn $3d$ and $1s$ core-hole states, $3p$ core-hole states, respectively. The Hamiltonian $H_{\text{multiplet}}$ describes the intra-atomic multiplet coupling originating from the multipole components of the Coulomb interaction between Mn $3d$ states and that between Mn $3d$ and $3p$ or $1s$ states. The spin-orbit interactions for Mn $3d$ and $3p$ states are also included in $H_{\text{multiplet}}$.

The Hamiltonian describing dipole transition process (where $1s$ core electron is excited to the p-symmetric conduction band around the core-hole site) is given by

$$H'=H+\sum_{k,\sigma}\varepsilon_{k,\sigma}c^{\dagger}_{k,\sigma}c_{k,\sigma}-\frac{u}{N}\sum_{k,k,\sigma}a^{\dagger}_{k,\sigma}a_{k',\sigma}, \tag{3.2}$$

where $\varepsilon_{k,\sigma}$ represents the energy of the p-symmetric conduction band and N is a number of unit cells of the MnF_2 crystals. The second term in Eq. (3.2) represents the effect of the core-hole potential on the conduction band. Here, we assume that the potential is of short range, and disregard the difference of u in the $1s$ and $3p$ core holes. More details can be found in Refs. 22 and 23.

The absorption spectrum due to the quadrupole transition is given as

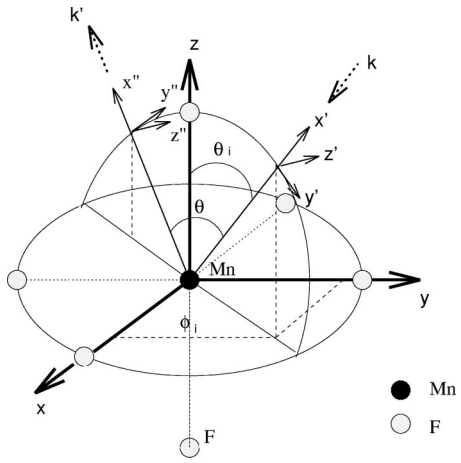

FIG. 2. Geometrical arrangement giving the coordinate of incident photon (x',y',z'), emitted photon (x'',y'',z'') and MnF_6^{-4} cluster (x,y,z).

$$I_{\mathrm{Q}}(\Omega)=\sum_{f}|\langle f|T^{(a)}_{\text{quadrupole}}|g\rangle|^2\frac{\Gamma_K/\pi}{(\Omega-E_f+E_g)^2+\Gamma_K^2}, \tag{3.3}$$

and $K\beta$ RXES due to the quadrupole transition in the absorption process is calculated on the basis of the formula of the coherent second order optical process as

$$\begin{aligned} S_{\mathrm{Q}}(\Omega,\omega)=&\sum_{p=y'',z''}\sum_{f}\\ &\times\left|\sum_{i}\frac{\langle f;p|T^{(e)}_{\text{dipole}}|i;0\rangle\langle i;0|T^{(a)}_{\text{quadrupole}}|g;y'\rangle}{E_g+\Omega-E_i-i\Gamma_K}\right|^2\\ &\times\frac{\Gamma_M/\pi}{(E_g+\Omega-E_f-\omega)^2+\Gamma_M^2}, \end{aligned} \tag{3.4}$$

where $|g\rangle$, $|i\rangle$, and $|f\rangle$ are the ground, intermediate, and final states of the Hamiltonian H with energies E_g, E_i, and E_f, respectively. The incident and emitted photon energies are represented by Ω and ω, respectively. The core-hole lifetime broadening are denoted by Γ_K for the $1s$ core hole and Γ_M for the $3p$ core hole. As shown in Fig. 2, we take into account the effect of the polarization of the incident photon and the effect of the angle between the incident photon and emitted photon. The direction of the incident photon wave vector $\mathbf{k}$ is denoted by incident angles θ_i and ϕ_i. The scattering angle between the incident and emitted photon directions, $\mathbf{k}$ and $\mathbf{k}'$, is denoted by θ. The polarization direction of the incident photon is in the plane of $\mathbf{k}$ and $\mathbf{k}'$, while the polarization of the emitted photon is not analyzed. We take xyz, $x'y'z'$, and $x''y''z''$ coordinate systems to be those fixed on the MnF_6^{-4} cluster, the incident photon, and the emitted photon, respectively. The directions of x, y, and z axis are taken in the three orthogonal Mn-F directions of the cluster. Here, we represent the electronic system as $|\rangle$, and the photon as $|\}$, so that the total system consisting of the electron and photon systems is represented by the direct product $|;\rangle\equiv|\rangle\otimes|\}$. According to the experimental geometry, the initial state of the total system is expressed as $|g;y'\rangle\equiv|g\rangle\otimes|y'\}$ with the electronic ground state $|g\rangle$ and a

y'-polarized photon $|y'\}$. Similarly, the intermediate and final state of RXES are written as $|i;0\rangle$ and $|f;p\rangle$, respectively, where $|0\}$ is the zero-photon state and $|p\}$ is the emitted photon state. For $|p\}$, we take all the independent polarizations of the emitted photon, namely, $|p\}$ is taken to be $|y''\},|z''\}$.

The operator $T^{(a)}_{\text{quadrupole}}$ represents the quadrupole transition from Mn $1s$ to $3d$ states by incident photon and $T^{(e)}_{\text{dipole}}$ is the dipole transition operator from Mn $3p$ to $1s$ states. They are expressed, using the spherical tensor operator $C^{(1)},C^{(2)}$, in the form

$$T^{(e)}_{\text{dipole}}=\hat{\mathbf{e}}'_{\mathbf{k}'}\cdot\mathbf{r}=\mathbf{r}\{\mathbf{e}'^{(+)}\mathbf{C}^{(1)}_1+\mathbf{e}'^{(-)}\mathbf{C}^{(1)}_{-1}+\mathbf{e}'^{(0)}\mathbf{C}^{(1)}_0\} \tag{3.5}$$

and

$$\begin{aligned}T^{(a)}_{\text{quadrupole}}&=(\hat{\mathbf{e}}_{\mathbf{k}}\cdot\mathbf{r})(\mathbf{k}\cdot\mathbf{r})\\&=r^2\Bigg\{\sqrt{\frac{2}{3}}k^{(-)}e^{(-)}C^{(2)}_2\\&\quad+\sqrt{\frac{2}{3}}k^{(+)}e^{(+)}C^{(2)}_{-2}\\&\quad+\sqrt{\frac{1}{3}}(-k^{(0)}e^{(-)}-e^{(0)}k^{(-)})C^{(2)}_1\\&\quad+\sqrt{\frac{1}{3}}(-k^{(0)}e^{(+)}-e^{(0)}k^{(+)})C^{(2)}_{-1}\\&\quad+k^{(0)}e^{(0)}C^{(2)}_0\Bigg\}.\end{aligned} \tag{3.6}$$

Here, $\hat{\mathbf{e}}'_{\mathbf{k}'}$ and $\hat{\mathbf{e}}_{\mathbf{k}}$ are unit vectors in the photon polarization directions, where $\mathbf{k}'$ and $\mathbf{k}$ are wave vectors of emitted and incident photons, respectively. $e^{(\pm)},e^{(0)}$ and $k^{(\pm)},k^{(0)}$ are defined by $e^{(\pm)}\equiv\mp1/\sqrt{2}(e_x\pm ie_y),e^{(0)}\equiv e_z$ and $k^{(\pm)}\equiv\mp1/\sqrt{2}(k_x\pm ik_y),k^{(0)}\equiv k_z$, respectively. $C^{(k)}_q$ is defined by

$$C^{(k)}_q\equiv\sqrt{\frac{4\pi}{2k+1}}Y_{kq} \tag{3.7}$$

with the spherical harmonics Y_{kq}. Because the polarization and the direction of the incident photon are parallel in y' axis and x' axis, respectively, the components of the $\mathbf{e}$ and $\mathbf{k}$ of the incident photon are given by

$$\begin{cases}e_x=\cos\theta_i\cos\phi_i\\e_y=\cos\theta_i\sin\phi_i\\e_z=-\sin\theta_i\end{cases} \tag{3.8}$$

and

$$\begin{cases}k_x=-k\sin\theta_i\cos\phi_i\\k_y=-k\sin\theta_i\sin\phi_i\\k_z=-k\cos\theta_i.\end{cases} \tag{3.9}$$

Similarly, the components of $\mathbf{e}'$ and $\mathbf{k}'$ of the emitted photon are given by

$$\begin{cases}e'_x=\cos(\theta-\theta_i)\cos\phi_i\delta_{py''}-\sin\phi_i\delta_{pz''}\\e'_y=\cos(\theta-\theta_i)\sin\phi_i\delta_{py''}+\cos\phi_i\delta_{pz''}\\e'_z=\sin(\theta-\theta_i)\delta_{pz''}\end{cases} \tag{3.10}$$

and

$$\begin{cases}k'_x=-k\sin(\theta-\theta_i)\cos\phi_i\\k'_y=-k\sin(\theta-\theta_i)\sin\phi_i\\k'_z=k\cos(\theta-\theta_i).\end{cases} \tag{3.11}$$

In Eq. (3.10) δ_{ij} represents the Kronecker delta. By substituting these components in Eqs. (3.5) and (3.6), each transition-matrix elements are given by

$$T^{(e)}_{\text{dipole}}=\sum_q\ r\times\{B_{1q}(\theta_i,\phi_i,\theta)C^{(1)}_q\}, \tag{3.12}$$

$$T^{(a)}_{\text{quadrupole}}=\sum_q\ \frac{1}{\sqrt{6}}r^2k\times\{A^{y'}_{2q}(\theta_i,\phi_i)C^{(2)}_q\}, \tag{3.13}$$

where the angle-dependent factors $B_{1q}(\theta_i,\phi_i,\theta)$ and $A^{y'}_{2q}(\theta_i,\phi_i)$ are given by

$$\begin{aligned}&B_{1q}(\theta_i,\phi_i,\theta)\\&=\begin{cases}\dfrac{1}{\sqrt{2}}e^{i\phi_i}\{-\cos(\theta-\theta_i)\delta_{py''}-i\delta_{pz''}\}, & q=1\\[2ex]\dfrac{1}{\sqrt{2}}e^{-i\phi_i}\{\cos(\theta-\theta_i)\delta_{py''}-i\delta_{pz''}\}, & q=-1\\[2ex]\sin(\theta-\theta_i)\delta_{py''}, & q=0\end{cases}\end{aligned} \tag{3.14}$$

and

$$A^{y'}_{2q}(\theta_i,\phi_i)=\begin{cases}-\sin\theta_i\cos\theta_ie^{-i2\phi_i}, & q=2\\-\sin\theta_i\cos\theta_ie^{i2\phi_i}, & q=-2\\e^{-i\phi_i}\cos2\theta_i, & q=1\\-e^{i\phi_i}\cos2\theta_i, & q=-1\\\sqrt{6}\cos\theta_i\sin\theta_i, & q=0.\end{cases} \tag{3.15}$$

The XAS due to the dipole transition is given by replacing the transition operator $T^{(a)}_{\text{quadrupole}}$ with $T^{(a)}_{\text{dipole}}$ in Eq. (3.3).

$$I_{\text{D}}(\Omega)=\int d\epsilon\rho(\epsilon)\sum_f\ |\langle f|T^{(a)}_{\text{dipole}}|g\rangle|^2\times\frac{\Gamma_K/\pi}{(\Omega-\epsilon-E_f+E_g)^2+\Gamma_K^2}, \tag{3.16}$$

where $|g\rangle$ and $|f\rangle$ are the ground and final states of XAS with energies E_g and E_f, respectively. The integral with respect to ϵ is taken over the high-energy continuum with the density of states $\rho(\epsilon)$. In a similar way, $K\beta$ RXES due to the dipole process is given as

$$S_{\mathrm{D}}(\Omega,\omega)=\int d\epsilon\rho(\epsilon)\sum_{p=y'',z''}\sum_{f}\times\left|\sum_{i}\frac{\langle f;p|T^{(e)}_{\mathrm{dipole}}|i;0\rangle\langle i;0|T^{(a)}_{\mathrm{dipole}}|g;y'\rangle}{E_g+\Omega-\epsilon-E_i-i\Gamma_K}\right|^2\times\frac{\Gamma_M/\pi}{(E_g+\Omega-\epsilon-E_f-\omega)^2+\Gamma_M^2}. \quad (3.17)$$

The transition operator $T^{(a)}_{\mathrm{dipole}}$ is given as

$$T^{(a)}_{\mathrm{dipole}}=\sum_{q} r\times\{A^{y'}_{1q}(\theta_i,\phi_i)C^{(1)}_q\}, \quad (3.18)$$

where the angle factor $A^{y'}_{1q}(\theta_i,\phi_i)$ is given by

$$A^{y'}_{1q}(\theta_i,\phi_i)=\begin{cases}-\frac{1}{\sqrt{2}}e^{-i\phi_i}\cos\theta_i, & q=1\\ \frac{1}{\sqrt{2}}e^{i\phi_i}\cos\theta_i, & q=-1\\ -\sin\theta_i, & q=0.\end{cases} \quad (3.19)$$

As we mentioned in Sec. II, our sample is powder, thus the spectral functions have to be integrated over θ_i and ϕ_i. Finally, the total spectra, I_{XAS} and S_{RXES}, are given as

$$I_{\mathrm{XAS}}(\Omega)=\int_0^{2\pi}d\phi_i\int_0^{\pi}d\theta_i\{I_{\mathrm{Q}}(\Omega)+I_{\mathrm{D}}(\Omega)\}, \quad (3.20)$$

$$S_{\mathrm{RXES}}(\Omega,\omega)=\int_0^{2\pi}d\phi_i\int_0^{\pi}d\theta_i\{S_{\mathrm{Q}}(\Omega,\omega)+S_{\mathrm{D}}(\Omega,\omega)\}. \quad (3.21)$$

IV. CALCULATED RESULTS

Here, we calculate the pre-edge of Mn K-XAS and the Mn $K\beta$ RXES for MnF_2. In order to diagonalize the Hamiltonian H, we use, as the basis states, three configurations, $3d^5$, $3d^6\underline{L}$, and $3d^7\underline{L}^2$, where $\underline{L}$ represents a hole in the ligand states. We denote the charge transfer (CT) energy from the ligand to $3d$ states as Δ. The energy difference between the three configurations are given, in the limit of $V\rightarrow 0$, as $E(d^6\underline{L})-E(d^5)=\Delta$ and $E(d^7\underline{L}^2)-E(d^6\underline{L})=\Delta+U_{dd}$, where $\bar{E}(d^7\underline{L}^2)$, $E(d^6\underline{L})$, and $E(\bar{d}^5)$ represent the configuration averaged energies. The intermediate states and final states of the quadrupole transition (dipole transition) are given by linear combinations of $1s^13d^6$, $1s^13d^7\underline{L}$, and $1s^13d^8\underline{L}^2$ ($1s^13d^54p$, $1s^13d^6\underline{L}4p$, and $1s^13d^7\underline{L}^2\bar{4p}$) configurations and $3p^53d^6$, $\bar{3p}^53d^7\underline{L}$, and $\bar{3p}^53d^8\underline{L}^2$ ($3p^53d^54p$, $3p^53d^6\underline{L}4p$, and $3p^53\bar{d}^7\underline{L}^24p$) configurations, respectively. The parameter values used are as follows: $U_{dc}(1s)=-8.3$, $U_{dc}(3p)=-7.3$, $V(e_g)=2.0$, $U_{dd}=7.2$, $\Delta=9.5$ in units of eV. For the hybridization, we use the empirical relation: $V(e_g)=-2V(t_{2g})$ according to Harrison.[26] The Slater integrals and the spin-orbit coupling constants are calculated by Cowan's Hartree-Fock program,[27] and then the Slater integrals are scaled down to 75%. The lifetime broadening of the $1s$ core-hole Γ_K is taken to be 0.6 eV [half width at half maximum (HWHM)] and the lifetime broadening of the $3p$ core hole Γ_M is taken to be the term-dependent $\Gamma_M(-0.1\omega)$ with the same values as those of Refs. 22 and 23. The importance of the term-dependent Γ_M has already been pointed out by several authors,[22,23,28,29] who showed that Γ_M strongly depends on the multiplet states by the super-Coster-Kronig decay process. Gaussian broadening due to the experimental resolution is taken to be 0.25 eV (HWHM). With the parameter values given above, the ground state is a mixed state of the three configurations with mixing weights 93.2% ($3d^5$),6.7% ($3d^6\underline{L}$),0.1% ($3d^7\underline{L}^2$). For the relative strength between the quadrupole and dipole transitions and their relative energy position, we use the same values as those estimated in Ref. 23, which were obtained from the analysis of the experimental excitation spectra. The quadrupole transition gives rise to a weak prepeak and the dipole transition gives rise to a broad background in XAS.

A. Comparison of experimental results and calculations

The result of the Mn K-XAS in the pre-edge region is shown in Fig. 3(a) together with the experimental results. In the pre-edge region of XAS, we can see a broad background due to the dipole transition ($1s\rightarrow 4p$) and a double-peak structure with an energy splitting of about 0.7 eV: namely, (A) peak is a t_{2g} symmetry peak and (B) peak is an e_g symmetry one. The corresponding energy separation is given by the e_g-t_{2g} splitting, $10Dq$.[15] While the calculated result yields the peak position in reasonable agreement with the experimental result, their amplitudes are at variance. If we change the intensity ratio between dipole and quadrupole contributions, we could reproduce the experimental amplitudes of these peaks, but there is no essential change in RXES.

The results of $K\beta$ RXES calculation are shown in Fig. 3(b), where the spectra (A) and (B) are obtained by tuning the incident photon energy to the energy positions (A) and (B) in Fig. 3(a). The spectrum NXES is obtained with the incident photon energy well above the threshold. The experimental NXES result is that for $\Omega=6600$ eV in Fig. 1(c). As we will show later, the spectral shape (as a function of ω) is independent of the incident photon energy Ω, if Ω is well above the threshold.

The solid lines describe the theoretical results, where the incident photon polarization is taken in the scattering plane (i.e., in the y' direction), the scattering angle θ is 90°, and the calculated spectra are averaged over θ_i and ϕ_i in consistency with the experimental geometry and the powdered sample. The model calculation and the experimental results are in good agreement. In both (A) and (B) spectra, we can see a double-peak structure with the energy splitting of about 0.7 eV and a broad satellite on the lower energy side, but a weak shoulder just below the double peaks is missing in the calculated result (for unknown reason). The double-peak structure is due to the mutiplet interaction between $3d$ and $3p$ electrons by quadrupole transitions. The broad satellite on the lower-energy side is not due to the exchange interaction between $3p$ and $3d$ electrons but due to the dipole transition.

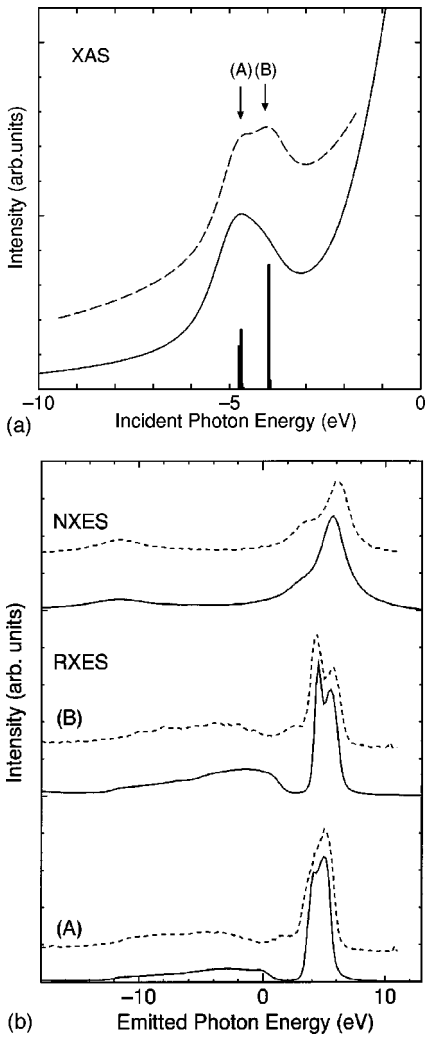

FIG. 3. Theoretical (solid line) and experimental (dashed line) Mn K-edge XAS spectra for MnF_2 is shown in (a). Theoretical and experimental Mn $K\beta$ resonant x-ray emission spectra for MnF_2 are shown in (b). The results $(A),(B)$ of RXES are obtained by tuning the incident photon energy to $(A),(B)$ of the XAS. (C) corresponds to $K\beta$ normal emission spectra.

Here, let us consider only the quadrupole contribution of RXES. As we mentioned before, only $1s$ down spin electron can be excited to the $3d$ states. In the intermediate state of RXES, the $1s$ down spin hole remains because of very weak interactions between $1s$ and $3d$ electrons. In the emission process $(3p\rightarrow 1s)$, only $3p$ down spin electron can make a radiative transition to $1s$ down spin hole. In the final state of $K\beta$ RXES, five $3d$ states with up spin and one $3d$ state with down spin are occupied and the hole of $3p$ state has a down spin. In this case, $3p$ and $3d$ electrons cannot change the spin through the exchange interaction between $3p$ and $3d$ electrons. As a result, the spectra due to the quadrupole transition do not have the exchange splitting satellite.

B. Angle dependence of the quadrupole contribution

In this section, we give a theoretical prediction on the incident angle dependence of the Mn $K\beta$ RXES in a single crystal sample of MnF_2. In general, the Mn $K\beta$ RXES depends on the incident angle, the emitted angle, and the polarization of the incident and emitted photons. This angle and polarization dependence is different for quadrupole and dipole excitations, so that it can be used as a means to distinguish the quadrupole and dipole excitations in the pre-edge of Mn K-XAS.

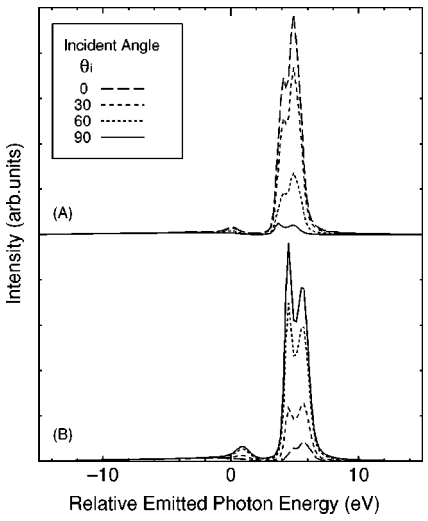

FIG. 4. Calculated results of the incident angle-dependent Mn $K\beta$ RXES of a MnF_2 single crystal. The angle ϕ_i is fixed to 45°. A and B are obtained by tuning the incident photon energy to (A) and (B) of the XAS in Fig. 3(a).

Let us consider the Mn $1s$-$3d$ quadrupole excitation in a MnF_2 single crystal. We calculate $K\beta$ RXES by changing the angle θ_i, where both ϕ_i and θ_e $(=\theta-\theta_i)$ are fixed to 45°, and the incident photon polarization is taken in the z' direction (the emitted photon polarization is not analyzed). Then the angle factor in the transition operator $T^{(a)}_{\text{quadrupole}}$ is given by

$$A^{z'}_{2q}(\theta_i,\phi_i)=\begin{cases}\sin\theta_i, & q=2\\ \sin\theta_i, & q=-2\\ -(1/\sqrt{2})(1+i)\cos\theta_i, & q=1\\ (1/\sqrt{2})(1-i)\cos\theta_i, & q=-1\\ 0, & q=0.\end{cases} \tag{4.1}$$

The calculated result is shown in Fig. 4. It is seen that the spectrum depends strongly on θ_i not only in the intensity but also in the spectral shape. The relative intensity of two main peaks in the spectra are clearly changing with incident angle θ_i.

Here, it should be remarked that if we assume the pre-edge XAS is not due to the quadrupole transition but due to the dipole transition, then the present Mn $K\beta$ RXES will not depend on θ_i both in the intensity and the spectral shape. This is because both $T^{(a)}_{\text{dipole}}$ and $T^{(e)}_{\text{dipole}}$ do not depend on θ_i (note that $T^{(a)}_{\text{dipole}}$ does not depend on θ_i because the incident photon polarization is always fixed in the z' direction).

In many transition metal compounds, a pre-edge structure is observed in the K-XAS, but its origin (quadrupole or dipole transition) is sometimes not very clear. For example, in TiO_2 the coexistence of quadrupole and dipole transitions was proposed, but an interpretation only by dipole transition

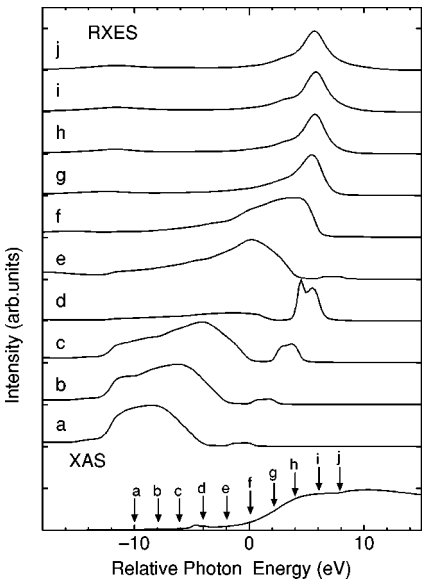

FIG. 5. Theoretical Mn $K\beta$ resonant x-ray emission spectra for MnF_2 at wide energy range of incident photon. The lowest spectra is Mn *K*-edge x-ray absorption spectra. The results **a**~**j** of RXES are obtained by tuning the incident photon energy at **a**~**j** of XAS.

was also given.[30–32] For Fe_2O_3, the relative intensity between the quadrupole and dipole transitions does not seem to be well established.[15,33] As is well known, the angle and polarization dependence in the intensity of XAS is different for quadrupole and dipole transitions, so that it has been used in order to distinguish the quadrupole and dipole transitions. However, in the case of RXES both the intensity and spectral shape of quadrupole contribution strongly depend on the incident angle θ_i, while the dipole contribution is constant. Therefore, the RXES provides us with more information on the difference of quadrupole and dipole transitions than XAS, and it will be a powerful tool to distinguish them.

C. Relation between RXES and NXES

In order to illustrate the relation between RXES and NXES we show in Fig. 5 the calculated Mn $K\beta$ RXES, which covers a wide range of incident photon energy. These results are obtained for a single-crystal MnF_2 and the incident angle and the scattering angle are fixed to $\theta_i = 45°$, $\phi_i = 0°$, and $\theta = 90°$. The RXES of **a**~**j** are calculated by setting the incident photon energy Ω at the XAS energy positions **a**~**j** (see the bottom of Fig. 5), respectively. All of these spectra are normalized so that the highest intensity of each spectrum is the same. The spectrum **d** in Fig. 5 is a single-crystal version of the spectrum (*B*) in Fig. 3(b).

From Fig. 5, we can see that, as the incident photon energy is increased, the spectrum changes from RXES (dispersing structure) to NXES (nondispersing structure). In the range of low incident photon energy (from **a** to **f**) the spectral shape depends strongly on the incident photon energy, but for high-energy region (from **g** to **j**), the spectral shape is independent of the incident photon energy, which is the characteristic feature of NXES. It is to be noted that the calculated result for **f** corresponds to the experimental one for *C* ($\Omega = 6545$ eV in Fig. 1(c), and the dispersive nature of the experimental spectra is nicely reproduced by this calculation.

V. CONCLUSION

Summarizing, we have presented the measurements of x-ray absorption and resonant x-ray emission spectra at the *K* pre-edge of Mn in a powdered MnF_2 sample and performed the theoretical calculations of these spectra with MnF_6^{-4} cluster model taking into account the intra-atomic multiplet effect and interatomic hybridization. The agreement between the experimental results and our calculation are very good.

Moreover, we have presented that resonant x-ray emission spectra have a strong sensitivity to the polarization and angle of the incident photon. This clearly demonstrates that important information to distinguish the quadrupole and dipole transitions can be obtained from the angle and polarization dependence of resonant x-ray emission spectra.

Finally, we have illustrated the relation between resonant x-ray emission spectra and normal x-ray emission spectra by setting the incident photon energy at a wide range of energy in XAS.

ACKNOWLEDGMENTS

The authors would like to thank Dr. H. Ogasawara for valuable discussions. This work was partially supported by a Grant-in-Aid for Scientific Research from the Ministry of Education, Science, Culture and Sports in Japan. The computation in this work was done using the facilities of the Supercomputer Center, Institute for Solid State Physics, the University of Tokyo. One of the authors (M. T.) would like to acknowledge the Canon Foundation for financial support.

[1] P.W. Anderson, Phys. Rev. Lett. **18**, 1049 (1967).
[2] P. Nozières and C.T. de Dominicis, Phys. Rev. **178**, 1097 (1969).
[3] A. Kotani and Y. Toyozawa, J. Phys. Soc. Jpn. **35**, 1073 (1973); **35**, 1082 (1973); **37**, 912 (1974).
[4] O. Gunnarsson and K. Schönhammer, Phys. Rev. B **28**, 4315 (1983).
[5] A. Fujimori and F. Minami, Phys. Rev. B **30**, 957 (1984).
[6] J. Zaanen, G.A. Sawatzky, and J.W. Allen, Phys. Rev. Lett. **55**, 418 (1985).
[7] S. Tanaka and A. Kotani, J. Phys. Soc. Jpn. **62**, 464 (1993).
[8] S.M. Butorin, D.C. Mancini, J.-H. Guo, N. Wassdahl, and J. Nordgren, J. Alloys Compd. **225**, 230 (1995).
[9] S.M. Butorin, D.C. Mancini, J.-H. Guo, N. Wassdahl, J. Nordgren, M. Nakazawa, S. Tanaka, T. Uozumi, A. Kotani, Y. Ma, K.E. Myano, B.A. Karlin, and D.K. Shuh, Phys. Rev. Lett. **77**, 574 (1996).
[10] S. M. Butorin, J.-H. Guo, D. K. Shuh, A. Kotani, and J. Nordgren (unpublished).
[11] M.H. Kirsch, F. Sette, U. Bergmann, C. Masciovecchio, R. Verbeni, J. Goulon, W. Caliebe, and C.C. Kao, Phys. Rev. B **54**, R12 673 (1996).
[12] J.-J. Gallet, J.-M. Mariot, C.F. Hague, F. Sirotti, M. Nakazawa,

H. Ogasawara, and A. Kotani, Phys. Rev. B **54**, R14 238 (1996).
[13] M. Nakazawa, S. Tanaka, T. Uozumi, and A. Kotani, J. Phys. Soc. Jpn. **65**, 2303 (1996).
[14] M. Nakazawa, Ph.D. thesis, University of Tokyo, 1997.
[15] W.A. Caliebe, C.-C. Kao, J.B. Hastings, M. Taguchi, A. Kotani, T. Uozumi, and F.M.F. de Groot, Phys. Rev. B **58**, 13 452 (1998).
[16] K. Hämäläinen, D.P. Siddons, J.B. Hastings, and L.E. Berman, Phys. Rev. Lett. **67**, 2850 (1991).
[17] K. Hämäläinen, C.-C. Kao, J.B. Hastings, D.P. Siddons, L.E. Berman, V. Stojanoff, and S.P. Cramer, Phys. Rev. B **46**, 14 274 (1992).
[18] S. Tanaka, K. Okada, and A. Kotani, J. Phys. Soc. Jpn. **63**, 2780 (1994).
[19] G. Peng, X. Wang, C.R. Randall, J.A. Moore, and S.P. Cramer, Appl. Phys. Lett. **65**, 2527 (1994).
[20] F.M.F. de Groot, A. Fontaine, C.C. Kao, and M. Krisch, J. Phys.: Condens. Matter **6**, 6875 (1994).
[21] X. Wang, C.R. Randall, G. Peng, and S.P. Cramer, Chem. Phys. Lett. **243**, 469 (1995).
[22] M. Taguchi and A. Kotani, J. Phys. Soc. Jpn. **65**, 706 (1996).
[23] M. Taguchi, T. Uozumi, and A. Kotani, J. Phys. Soc. Jpn. **66**, 247 (1997).
[24] X. Wang, F.M.F. de Groot, and S.P. Cramer, Phys. Rev. B **56**, 4553 (1997).
[25] W.A. Caliebe, C.-C. Kao, M. Krisch, T. Oversluizen, P. Montanez, and J.B. Hastings, in *Synchrotron Radiation Instrumentation: The Tenth US National Conference, Ithaca, New York*, edited by E. Fontes, AIP Conf. Proc. No. **417** (AIP, New York, 1997), p.6.
[26] W. A. Harrison, *Electronic Structure and the Properties of Solids* (Freeman, San Francisco, 1980).
[27] R. Cowan, *The Theory of Atomic Structure and Spectra* (University of California Press, Berkeley, 1981).
[28] K. Okada, A. Kotani, H. Ogasawara, Y. Seino, and B.T. Thole, Phys. Rev. B **47**, 6203 (1993).
[29] H. Ogasawara, A. Kotani, and B.T. Thole, Phys. Rev. B **50**, 12 332 (1994).
[30] R. Brydson, H. Sauer, W. Engel, J.M. Thomas, E. Zeitler, N. Kosugi, and H. Kuroda, J. Phys.: Condens. Matter **1**, 797 (1989).
[31] C. Brouder, J.P. Kappler, and E. Beaurepaire, *Proceedings of the 2nd European Conference on Progress in X-ray Synchrotron Radiation Research*, Rome, 1989 (SIF, Bologna, 1990).
[32] T. Uozumi, K. Okada, A. Kotani, O. Durmeyer, J.P. Kappler, E. Beaurepaire, and J.C. Parlebas, Europhys. Lett. **18**, 85 (1992).
[33] G. Dräger, R. Frahm, G. Materlik, and O. Brümmer, Phys. Status Solidi B **146**, 287 (1988).